Chronic optogenetic activation of hippocampal pyramidal neurons replicates the proteome footprint of Alzheimer's disease-like pathology

Authors:

Iason Keramidis[1,2], Martina Samiotaki[3], Romain Sansonetti[1], Johanna Alonso[1], Katerina Papanikolopoulou[4], Yves De Koninck[1,2]

Affiliations:

[1]CERVO Brain Research Centre, Quebec Mental Health Institute, Québec, QC, Canada.
[2]Department of Psychiatry & Neuroscience, Université Laval, Québec, QC, Canada.
[3]Institute for bio-Innovation, Biomedical Sciences Research Center Alexander Fleming, Vari, Greece.
[4]Institute for Fundamental Biomedical Research, Biomedical Sciences Research Center Alexander Fleming, Vari, Greece.
[*]Corresponding author. Email: yves.dekoninck@neuro.ulaval.ca

Abstract

Neuronal overexcitability can elicit synaptic changes, leading to neuronal hyperactivity and abnormal neural circuit processing. Such network disruption impairs neuronal function and survival, initiating neurodegeneration and Alzheimer's disease (AD). Yet, the sequence of synaptic changes resulting from excessive neuronal activity remains elusive. We employed optogenetics to induce sustained neuronal hyperactivity in the hippocampi of wild-type and AD-like 5xFAD mice. Surprisingly, after a month of daily optogenetic stimulation, the proteomic profiles of photoactivated wild-type and 5xFAD mice exhibited remarkable similarity. Proteins involved in translation, protein transport, autophagy, and notably in the AD pathology were upregulated in wild-type mice. Conversely, both glutamatergic and GABAergic synaptic proteins were downregulated. These hippocampal proteomic and signaling alterations in wild-type mice resulted in spatial memory loss and augmented Aβ42 secretion. Collectively, these findings indicate that sustained neuronal hyperactivity alone replicates proteome changes seen in AD-linked mutant mice. Therefore, prolonged neuronal hyperactivity may contribute to synaptic transmission disruption, memory deficits and the neurodegenerative process associated with AD.

Introduction

Aberrant neuronal activity can impair synapse formation and strength resulting in disruption of synaptic plasticity. In turn, altered synaptic plasticity could reorganize synaptic connections ensuing runaway excitation or quiescence and eventually modify local neuronal circuits (*1*). For neural circuits to maintain their characteristic firing patterns, neurons within the network undergo homeostatic changes at the cellular level, regulating synthesis and degradation of key synaptic proteins (*2*, *3*). Alterations perturbing these regulations have been linked with the onset of various brain disorders such as epilepsy and autism (*4*).

Neuronal hyperexcitability manifests early in Alzheimer's disease (AD) (*5*–*7*), leading to cortical and hippocampal hyperactivity (*8*, *9*) and under certain conditions to epileptiform activity and seizures in rodents (*10*, *11*) and humans (*12*). Both amyloid-β (Aβ) and Tau have been found to induce neuronal hyperactivity through distinct cellular mechanisms (*11*, *13*–*16*). Concurrently, neuronal hyperactivity can increase Aβ secretion (*17*, *18*) and promote pathological phosphorylation of Tau (*19*). These observations suggest that Aβ and Tau can initiate a vicious cycle of neuronal hyperactivity in AD underlying neurodegeneration in disease. However, it remains unknown whether neuronal hyperactivity alone can induce pathology mimicking neurodegeneration in AD.

Optogenetics has emerged as a powerful method to control the activity of genetically defined neurons allowing to study the function of selective brain circuits in physiological but also pathological conditions (*20*–*22*). Stabilized step function opsins (SSFOs) allow also for long-lasting activation of neural circuits with just a brief light stimulation (*23*). Such chronic optogenetic activation is necessary to model neurodegenerative disorders like AD for which neuronal activity is altered for long periods of time. We adopted a similar approach to generate a model of chronic neuronal hyperactivity in the hippocampus of wild-type (WT) and a transgenic mouse line carrying AD-linked mutations and demonstrated that evoked neuronal hyperactivity can disrupt synaptic signalling and facilitate an activity-driven neuropathology similar to AD.

Results

Optogenetic activation of the hippocampus in wild-type and 5xFAD mice using SSFO

To generate a model of chronic neuronal hyperactivity in the rodent hippocampus we virally transduced the SSFO-mCherry or tdTomato unilaterally under the CaM kinase II promoter (CaMKIIa) into the CA1 of WT or 5xFAD (*24*) male mice (Fig. 1A, B). We then inserted an optic fiber cannula above the CA1 and stimulated the infected neurons for 4 weeks by blue light (Fig. 1A). To validate whether light stimulation of the SSFO evoked neuronal activity, we performed both immunostaining and immunoblot analysis for c-Fos on brain sections or in hippocampal lysates, respectively. Coronal sections of mice infected with AAV-CaMKIIa-SSFO-mCherry in the hippocampus showed mCherry labelling in the CA1, CA2 and CA3 (Fig. 1B). Thirty minutes after light stimulation of mice expressing the SSFO-mCherry, the ipsilateral CA1, CA3 and dentate gyrus (DG) neurons displayed increased c-Fos as compared to neurons of the contralateral side (Fig. 1C). In mice infected with AAV-CaMKIIa-tdTomato, neurons in both hippocampus sides were negative for c-Fos (Supplementary Fig. S1). The c-Fos expression levels were significantly higher in hippocampal lysates from mice expressing SSFO as compared to tdTomato expressing mice (Supplementary Fig. S2).

Using extracellular recordings in anesthetized mice we assessed the light-induced changes in the activity of the CA1 region transduced either with the SSFO or tdTomato using a glass micro-optrode we previously designed, which enables dual, co-registered electrophysiological recording and optogenetic stimulation, free of photo-electric artefacts (Fig. 1D) (*25*, *26*). In mice expressing the SSFO, the multiunit spike rates within the CA1 increased for several minutes after a 2s light pulse as expected (Fig. 1E, F). Conversely, in tdTomato expressing mice, multiunit spiking activity did not increase following the brief light pulse (Fig. 1E, F). Altogether, these results indicate that the SSFO is transduced in the hippocampus and can be activated by light stimulation to generate neuronal hyperactivity.

Chronic optogenetic stimulation of the hippocampus activates protein translation and phosphorylation but downregulates synaptic proteins in wild-type mice

We sought to identify and quantify alterations in protein levels in response to sustain neuronal hyperactivity in the hippocampus of mice. We analyzed the hippocampi of WT mice expressing

56 SSFO or tdTomato after 4 weeks of daily brief light stimulation (Fig. 1A) using label-free liquid
57 chromatography with tandem mass spectrometry (LC-MS/MS) proteomic analysis. We identified
58 778 proteins differentially abundant (P value ≤ 0.05) between the two conditions (Fig. 2A;
59 Supplementary Table S1). The chronic optogenetic stimulation in mice expressing SSFO
60 significantly upregulated the expression of 556 proteins and only downregulated the expression of
61 222 proteins (Fig. 2A). Gene Ontology (GO) enrichment analysis with GeneCodis (*27*) revealed
62 that the abundant proteins were mainly part of the cytoplasmic and mitochondrial cellular
63 components (Fig. 2B). Yet, 77 of the proteins identified were part of the synapse (Fig. 2B) with
64 approximately 45% appearing downregulated, suggesting that synaptic function is altered by
65 evoked neuronal hyperactivity.

66 Moreover, GO analysis revealed that translation, protein transport, phosphorylation and
67 autophagy were among the most enriched biological processes found altered by the chronic
68 optogenetic stimulation (Fig. 2C). In turn, the AMPK signaling, and ubiquitin-mediated
69 proteolysis were identified among the top 10 most enriched KEGG pathways (Fig. 2D).
70 Surprisingly, the AD pathway was also identified, with 31 proteins, all found upregulated in the
71 WT+SSFO mice (Fig. 2D).

72 Out of the 34 downregulated synaptic proteins, interaction network analysis with STRING
73 (*28*), identified 19 proteins as glutamatergic synapse proteins, while 9 were enriched in
74 GABAergic synapses (Fig. 2E). And yet there are several more proteins, key for synaptic
75 transmission, which were found significantly downregulated in WT mice following chronic
76 hippocampal hyperactivity (Fig. 2E, F). Using immunoblots, we confirmed that Calbindin 1
77 (Calb1) was indeed downregulated in hippocampal lysates from WT+SSFO expressing mice as
78 compared to WT+tdTom mice (Fig. 2G, H). Additionally, the excitatory amino acid transporter 1
79 (EAAT1 or Slc1a3) was downregulated, while the excitatory amino acid transporter 2 (EAAT2 or
80 Slc1a2) was unaltered in the WT+SSFO mice (Fig. 2G, H), consistent with the findings from the
81 proteomic analysis (Fig. 2A; Supplemental Table S1).

82 **Early AD pathology in 5xFAD mouse hippocampus largely mimics the footprint of altered**
83 **proteostasis caused by chronic optogenetic stimulation**

84 The 5xFAD mice exhibit amyloid deposition accompanied by cognitive deficits recapitulating
85 major features of Alzheimer's disease amyloid pathology (*29*). Comparison of AD human and

86 rodent brain tissue revealed that the 5xFAD mice exhibit a proteomic signature similar to
87 symptomatic AD (*30*). Moreover, an independent analysis of the mouse hippocampal proteome
88 focused on the proteomic changes during progression of the amyloid pathology (*31*). In turn, we
89 analyzed the proteome changes manifesting in 3-month-old 5xFAD mice, to identify similarities
90 between the pre-symptomatic AD brain and the effect of hippocampal neuronal hyperactivity in
91 WT mice.

92 When we compared the proteins altered by the mutations and the AD pathology in the
93 hippocampus of 5xFAD mice, we identified 926 proteins as differentially expressed (Fig. 3A;
94 Supplementary Table S2). The majority of these proteins were upregulated (Fig. 3B). Protein
95 translation and transport, autophagy and phosphorylation were identified among the altered
96 biological processes in the 5xFAD mice (Fig. 3C), consistent with our findings in the WT+SSFO
97 mice (Fig. 2C). The mitochondria, synapse and endosomes were among the most enriched cellular
98 components (Fig. 3D). The majority of the abundantly expressed synaptic proteins belong to the
99 glutamatergic synapse, with 61% of them found downregulated in 5xFAD mice (Fig. 3D).
100 Interestingly, for biological processes such as translation, phosphorylation, autophagy and RNA
101 slicing the common proteins between the WT+SSFO and 5xFAD mice showed more than 50%
102 overlap between the two groups (Fig. 4A), as well as the same valence (Fig. 4B). For the proteins
103 found in the synapse the overlap was at 45.5% (Fig. 4A) and only Arr3 showed contrasting valence
104 between the two groups (Fig. 4B). Finally, the GO analysis identified 38 proteins implicated in the
105 AD pathway in the presymptomatic 5xFAD mice (Fig. 3E, 4D), with 19 of them also found
106 abundantly expressed in WT+SSFO mice (Fig. 4B, C, E), indicating that chronic optogenetic
107 activation of the hippocampus in WT mice induced signalling cascades involved in the AD
108 pathogenesis.

109 **Evoked chronic neuronal hyperactivity in the hippocampus of 5xFAD mice downregulates**
110 **mRNA splicing and protein phosphorylation**

111 We adopted the same approach to induce neuronal hyperactivity in the hippocampus of 5xFAD
112 mice (Fig. 1A). The chronic optogenetic stimulation in 5xFAD mice resulted in significantly
113 downregulating the expression levels of 264 proteins while it resulted in upregulating the levels of
114 only 99 proteins (Fig. 5A; Supplementary Table S3). The altered proteins were primarily
115 cytoplasmic, nucleic and part of the spliceosomal complex (Fig. 5B). Among the cellular

116 components greatly enriched, the glutamatergic synapse was identified with 29 proteins (Fig. 5B),
117 83% of which were downregulated. Three additional proteins of the GABAergic synapse were
118 found downregulated in the 5xFAD mice after the chronic optogenetic stimulation (Fig. 5C).

119 Contrary to the WT mice, GO enrichment analysis revealed that neurons in 5xFAD mice
120 responded distinctly to the induced neuronal hyperactivity by downregulating mRNA processing,
121 splicing and protein phosphorylation (Fig. 5D). Consistently, the spliceosome and RNA
122 degradation appeared among the most enriched KEGG pathways in the 5xFAD+SSFO mice (Fig.
123 5E). The purine and pyrimidine metabolism pathways were also affected (Fig. 5E). Lastly,
124 biological processes such as chemical synaptic transmission and synapse organization appeared
125 altered (Fig. 5F) by the chronic optogenetic stimulation in the 5xFAD mice. These findings
126 indicate that the 5xFAD mice respond distinctively to the chronic stimulation, as compared to the
127 WT mice, and thus the plasticity mechanisms induced by the stimulation in WT mice matches the
128 changes occurring at early rather than late stages of the AD pathogenesis.

129 **Degree of similarity in proteome changes caused by hyperactivity in WT brain *vs*. that in**
130 **AD-related pathology**

131 Hippocampal hyperactivity has been implicated in memory deterioration and AD pathogenesis (*5*,
132 *12*). To further explore whether chronic optogenetic activation in the hippocampus of WT mice
133 indeed replicates some of the neurodegenerative processes involved in the pathogenesis of AD, we
134 performed a hierarchical clustering analysis based on our proteomic data. Accordingly, we found
135 that the WT+SSFO mice grouped together with the 5xFAD+tdTom while all the WT+tdTom mice
136 separated from the rest of mice according to the changes in protein levels (Fig. 6A). Moreover,
137 when we compared the proteins altered by stimulation in WT+SSFO mice to the ones altered due
138 to the mutations and AD-related pathology in the 5xFAD mice, we found that those two groups
139 resemble themselves much more than when comparing 5xFAD mice to unstimulated control (only
140 135 protein changes in common; Fig. 6B).

141 The mammalian target of rapamycin complex 1 (mTORC1) is a principal signalling
142 pathway controlling protein translation initiation (*32*) and has been postulated to take part in AD
143 pathology (*33*). Immunoblotting of hippocampal lysates revealed an increase in the
144 phosphorylation of the mTORC1 downstream translation initiation effector ribosomal protein S6

145 (rpS6; Fig. 6C, E), concomitant with an increase in the expression of Rheb (Fig. 6C, D), the
146 mTORC1 canonical activator (*34*) in the WT+SSFO mice as compared to the WT+tdTom mice.
147

148 **Neuronal hyperactivity in wild-type mice induces spatial memory deficits and augments**
149 **Aβ42 secretion**

150 To further examine how chronic hippocampal hyperactivity and the synaptic transmission changes
151 (Fig. 2F) observed following the optogenetic stimulation impact brain function, we performed
152 behavioral testing of WT and 5xFAD mice. We adopted a modified version of the Y-maze
153 alternation test allowing for the evaluation of spatial memory performance in mice (Supplementary
154 Fig. S3). We found that chronic optogenetic stimulation in the hippocampus of WT+SSFO mice
155 resulted in spatial memory deficits, similar to the impairment seen here in 6-months-old 5xFAD
156 mice (Fig. 6F), or previously described in (*35*).

157 Finally, since previous observations have linked neuronal and network hyperactivity with
158 an increase in the secretion and deposition of amyloid-β in the brain of transgenic mice carrying
159 several AD-linked mutations (*17*, *18*, *36*, *37*), we sought to measure the levels of soluble Aβ40
160 and Aβ42 in the brain of WT mice following our chronic optogenetic stimulation protocol. In the
161 hippocampus of WT+SSFO mice the levels of soluble secreted Aβ42 were significantly increased
162 as compared to the levels in the brain of WT+tdTom mice (Fig. 6G). The levels of Aβ40 showed
163 a trend of increase in the WT+SSFO mice, but this increase was not significantly different to the
164 Aβ40 levels in the WT+tdTom (Fig. 6G). Altogether, these results suggest that chronic neuronal
165 hyperactivity is sufficient to induce synaptic transmission disruption and memory loss similar to
166 that observed in the neurodegenerative process in AD, but also augments the amyloidogenic
167 cleavage of App.

168 Discussion

169 We adopted optogenetics and an SSFO to induce chronic neuronal hyperactivity and examine the
170 effect of such manipulation in the hippocampus of young WT and 5xFAD mice. We present
171 evidence of (i) an overt downregulation in the levels of both excitatory and inhibitory synaptic
172 proteins and an activation of translation, phosphorylation and autophagy following neuronal
173 hyperactivity in WT mice; (ii) an upregulation of AD-associated proteins in WT+SSFO mice
174 mimicking the AD proteome signature found in the 5xFAD mice; (iii) a downregulation in the

levels of proteins participating in RNA processing and protein phosphorylation in 5xFAD+SSFO mice; (iv) spatial memory impairments in WT+SSFO mice upon light stimulation; and (5) elevated levels of soluble Aβ42 in WT hippocampi following chronic optogenetic stimulation. These findings strongly support the notion that rampant neuronal hyperactivity distorts cellular mechanisms regulating proteostasis similar to that seen in the prodromal phase of AD-like pathology. This positions overt neuronal hyperactivity as a substrate of AD pathogenesis.

In various neurological disorders, cognitive decline has been associated with hippocampal hyperactivity and the failure to deactivate brain regions consisting of the default mode network (e.g. posterior cingulate cortex, precuneus, retrosplenial cortex) (*5*, *38–42*). Reducing neuronal hyperactivity pharmacologically has been also found to improve cognitive performance in humans with mild cognitive decline (*43*, *44*) suggesting that neuronal hyperactivity is a cause and not a compensatory mechanism of cognitive decline. But neuronal hyperactivity may have broader implications in disease onset. Apart from contributing to cognitive deficits, neuronal hyperactivity could drive several other pathological aspects related to AD, such as mTORC1 hyperactivity (*45*), Aβ release (*18*), synaptic loss (*46*, *47*) and neuronal degeneration (*38*).

It has been shown before that electrical, pharmacological and optogenetic neuronal stimulation can augment the secretion of Aβ from the presynaptic terminals in various APP transgenic mouse lines (*17*, *18*, *36*, *37*). In turn, elevated Aβ levels have been shown to induce neural overexcitability and hyperactivity disrupting neural circuits both in WT and APP transgenic mouse lines (*10*, *13*, *48*). Moreover, in humans, within the brain regions where Aβ aggregation is pronounced, the basal metabolic rates and neuronal activity are profoundly elevated (*8*, *37*, *49*). These findings support the hypothesis of a vicious unclamped cycle facilitating an Aβ-dependent neuronal hyperactivity in AD (*13*) and are in line with our results showing an increase in soluble Aβ42 secretion and a multifactorial perturbation of synaptic transmission in WT animals following neuronal hyperactivity.

The similarity we found in altered proteostasis and spatial memory in overstimulated WT and 5xFAD mice, together with the finding that neuronal hyperactivity in WT mice augments Aβ42 secretion establish chronic optogenetic stimulation in WT animals as a potential paradigm to model sporadic AD-pathogenesis.

Finally, the distinct response to the chronic optogenetic stimulation in the 5xFAD, at least at the proteome level, may reflect an occlusion of the detrimental effects of evoked neuronal

206 hyperactivity in AD, or a loss of proteostasis reserve. This is in line with observations indicating
207 that neuronal hyperactivity manifests early in AD resulting in synapse and circuit disruption (*5*, *6*,
208 *50*, *51*). And yet, while these deficits in circuits arising from neuronal degeneration in AD might
209 appear beyond repair, suppressing excessive neuronal activity early in the progression of the
210 disease may represent a possible therapeutic modality to delay or modify the disease progression
211 and cease the vicious cycle of relentless hyperactivity.

212 Materials and Methods

213 Animals

214 Rodent experiments were carried out on male 5xFAD mice, and their WT littermates bred and
215 housed in the CERVO Brain Research Centre animal facility. The male 5xFAD and female
216 B6SJLF1/J breeders were purchased from the Jackson Laboratory (#34840-JAX and #100012,
217 respectively). Mice were housed on a 12 h day/night cycle with ad libitum access to food and
218 water. Mice were randomly assigned to experimental groups. All experiments were approved by
219 the committee for animal protection of Université Laval (CPAUL) and followed the guidelines
220 from the Canadian Council for Animal Care.

221 Surgical Procedures and viral transduction

222 All viral constructs were produced by the CERVO Canadian Optogenetics and Vectorology
223 Foundry Core Facility (RRID: SCR_016477). The tip of the optic fiber (200 µm core, 0.39 NA on
224 2.5 mm ceramic ferrules) was coated with 100 nL of a 1:1 mix of silk fibroin solution (Sigma
225 5154-20ML) and the viral vector AAV2/5-CaMKIIa-hChR2(C128S/D156A)-mCherry
226 (henceforth referred to as AAV2/5-CaMKIIa-SSFO-mCherry; titer: 7.7 x 10^{12} GC/mL) or
227 AAV2/8-CaMKIIa-tdTomato (titer: 1.3 x 10^{13} GC/mL), prior to the surgery, and left to dry for 15
228 hrs at 4 °C as described in (*52*).

229 Stereotaxic surgeries were performed on mice (4-weeks old) maintained on isoflurane
230 anaesthesia (1.5%-2% in O2). Briefly, we removed the skin atop the cranium and a ~250-µm-
231 diameter craniotomy was drilled over the hippocampus at coordinates relative to Bregma of -2.30
232 mm rostro-caudal and -2.00 mm latero-medial. The optic fiber cannula was lowered 1.60 mm into
233 the brain (-1.60 mm dorso-ventral) and fixed on the cranium with C&B Metabond® (Parkell Inc.).

234 Following the surgery, mice were single-housed, and the chronic optogenetic stimulation
235 experiments started 4-5 weeks later.
236 For the optrode recordings, the same viral vectors were unilaterally infused into each side
237 of the hippocampal CA1 (rostro-caudal: -2.30 mm, latero-medial: 2.00 mm, dorso-ventral: 1.60
238 mm). The infusion was performed with pulled borosilicate glass capillaries and a
239 NANOLITER2020 injector (World Precision Instruments LLC). The in vivo optrode experiments
240 started a minimum of 4 weeks later.

241 **Optogenetic stimulation**

242 After 4-5 weeks from the optic fiber implantation mice were optically stimulated for 2 s every 24
243 hrs (starting at 2-months of age) for 4 weeks with blue light (470 nm, 1 mW). The light was
244 generated by an LED diode (ThorLabs M470F3) and delivered through fiber optics (200 µm core,
245 0.39 NA) to the implanted fiber optic cannulae.

246 ***In vivo* extracellular optrode recordings**

247 Simultaneous optical stimulation and electrical extracellular recording in the hippocampal CA1
248 was performed in WT male mice previously transduced with SSFO or tdTomato using a micro-
249 optrode (*25*). Briefly, mice were anesthetized with a mix of 100 mg ketamine, 15 mg xylazine and
250 2.5 acepromazine per kg and placed in a stereotaxic frame on a temperature control pad. A
251 craniotomy was drilled over the hippocampus at coordinates relative to Bregma of -2.30 mm
252 rostro-caudal and -2.00 mm latero-medial. A micro-optrode (6-8 µm tip diameter; 550 µm optical
253 core; 0.29 NA; 250 µm hollow core) was filled with 0.5 M potassium acetate solution, connected
254 to a 488 nm laser diode (Doric lenses) through a multimode optical fiber (200 µm optical core;
255 0.22 NA; ThorLabs) and lowered vertically to the brain. Electrophysiological recordings were
256 initiated at -1,3 mm ventral. A 2s long light pulse was delivered to activate the SSFO. The
257 extracellular electrophysiological signal was amplified (Neurodata IR183, Cygnus technology),
258 filtered (band pass, 300–3,000 Hz, model 440, Brownlee Precision), and digitized. The filtered
259 traces were analyzed with Spike2 (Cambridge Electronic Design). Events were detected and the
260 firing rate of individual neurons was plotted in peristimulus time histograms (PSTH) with 10 s
261 bins. Neurons for which the standard deviation of firing rate for the light pulse bin was 1.5 times

262 superior to the basal firing rate (average of the firing rate during the 60s preceding the pulse of
263 light) were considered activated.

264 **Sample Preparation**

265 For the proteomics analysis, brains were excised from anesthetized mice (30% urethane in saline)
266 within 30 min after optogenetic stimulation. The hippocampi were dissected, collected in sample
267 tubes, frozen immediately in liquid nitrogen, and stored at -80 °C until use. 25 mg of frozen tissue
268 was lysed in 150 µL of freshly made lysis buffer (4% SDS, 0.1 M DTT, 100 mM Tris/HCl; pH
269 7.6) and homogenized with an electric FisherBrandTM Pellet PestleTM homogenizer (Thermo
270 Fisher Scientific). Homogenates were incubated at 95 °C for 3 min and centrifuged at 16,000 g for
271 5 min. The supernatants were transferred into sample tubes and stored at -80 °C.

272 For ELISA and immunoblots, tissue was harvested as before within 30 min after
273 optogenetic stimulation. 25 mg of frozen hippocampus tissue was homogenized in 150 µL of RIPA
274 buffer (50 mM Tris-HCl, 150 mM NaCl, 1% Triton X-100, 0.5% Na deoxycholate, 0.1% SDS; pH
275 8.0). Homogenates were incubated under constant agitation for 4 hrs at 4 °C for lysis. Lysates were
276 centrifuged at 17,200 g and 4 °C for 10 min. Supernatants were collected and stored at -30 °C.

277 **Protein mass spectrometry**

278 Protein mass spectrometry analysis was performed in the Proteomics Facility of Biomedical
279 Sciences Research Centre Alexander Fleming. Four to five biological replicas for each condition
280 (WT + AAV2/8-CaMKIIa-tdTomato; WT + AAV2/5-CaMKIIa-SSFO-mCherry; 5xFAD +
281 AAV2/8-CaMKIIa-tdTomato; 5xFAD + AAV2/5-CaMKIIa-SSFO-mCherry) were analyzed.
282 Briefly, proteins of the lysed samples were processed according to the sensitive Sp3 protocol (*53*).
283 The reduced cysteine residues were alkylated in 200 mM iodoacetamide (Acros Organics). 20 µg
284 of beads (1:1 mixture of hydrophilic and hydrophobic SeraMag carboxylate-modified beads; GE
285 Life Sciences) were added to each sample in 50% ethanol. Protein clean-up was performed on a
286 magnetic rack. The beads were washed twice with 80% ethanol followed by one wash with 100%
287 acetonitrile (Fisher Chemical). The beads-captured proteins were digested overnight at 37 °C with
288 0.5 µg trypsin/LysC mix in 25 mM ammonium bicarbonate under vigorous shaking (1200 rpm,
289 Eppendorf Thermomixer). The supernatants were collected, and the peptides were purified by a
290 modified Sp3 clean-up protocol and finally solubilized in the mobile phase A (0.1% formic acid

291 in water), and sonicated. Peptides concentration was determined through absorbance measurement
292 at 280 nm using a nanodrop instrument.
293 Peptides were analyzed by a liquid chromatography tandem mass spectrometry (LS-
294 MS/MS) on a setup consisting of a Dionex Ultimate 3000 nanoRSLC online with a Thermo Q
295 Exactive HF-X Orbitrap mass spectrometer. Peptidic samples were directly injected and separated
296 on a 25 cm-long analytical C18 column (PepSep, 1.9 μm^3 beads, 75 µm ID) using a 90 min long
297 run. The full MS was acquired in profile mode using a Q Exactive HF-X Hybrid Quadropole-
298 Orbitrap mass spectrometer operating in the scan range of 375-1400 m/z using 120 K resolving
299 power with an Automatic Gain Control (AGC) of 3×10^6 and a max IT of 60 ms followed by data
300 independent analysis (DIA) using 8 Th windows (39 loops counts) with 15 K resolving power with
301 an AGC of 3×10^5, a max IT of 22 ms and normalized collision energy (NCE) of 26.

302 **Label-free quantification and data analysis**

303 Orbitrap raw data were analyzed in DIA-NN 1.8 (Data-Independent Acquisition by Neural
304 Networks) against the complete Uniprot Mus musculus proteome (Downloaded April 16, 2021)
305 supplemented with APP, presenilin, mCherry and ChR2. Search parameters were set to allow up
306 to two possible trypsin/P enzyme missed cleavages. A spectra library was generated from the DIA
307 runs and used to reanalyze them. Cysteine carbamidomethylation was set as a fixed modification
308 while N-terminal acetylation and methionine oxidations were set as variable modifications. The
309 match between runs (MBR) feature was used for all the analyses and the output (precursor) was
310 filtered at 0.01 false discovery rate (FDR). The protein inference was performed on the gene level
311 using only proteotypic peptides. The double pass mode of the neural network classifier was also
312 activated. Perseus (version 1.6.15.0) (*54*) was used for data processing and statistical analysis.
313 Proteins were subjected to filtering based on valid values setting a threshold of 70% valid values
314 in at least one group. Remaining missing values were imputed separately for each column (based
315 on the normal distribution using width of 0.3 and down shift of 1.8). The statistically significant
316 proteins were then Z-scored and visualized by Euclidean hierarchical clustering as heat maps.
317 Gene-Ontology analysis was performed with GeneCodis (*27*) by uploading the list of
318 altered proteins based on the T-test two-sample comparisons. The interaction network analysis of
319 functional or physical protein to protein associations were performed with STRING (version 11.5)
320 (*28*).

321 **Immunoblots**

322 Hippocampal lysates were diluted in Laemmli buffer at a concentration of 10 µg per 20 µL and
323 denaturized for 5 min at 95 °C. Proteins were separated in 4–15% Mini-PROTEAN® TGX Stain-
324 Free™ acrylamide gels (BioRad) and transferred onto 0.45 µm low-fluorescence PVDF
325 membranes (BioRad). Membranes were probed with the rabbit monoclonal anti-EAAT1 (Abcam
326 ab176557), anti-EAAT2 (Abcam ab205248), anti-S6 (Cell Signaling 2217), anti-S6 Ser240/244
327 (Cell Signaling 5364), anti-Rheb (Cell Signaling 13879), anti-c-Fos (Cell Signaling 2250) or the
328 rabbit polyclonal anti-Calbindin (Millipore ABN2192) in Tris-buffered saline containing 0.2%
329 Tween and 5% bovine serum albumin at 4 °C. All antibodies were used at 1:1000, except from the
330 anti-S6 Ser240/244 which was used at 1:10000. The appropriate anti-mouse or anti-rabbit IgG
331 conjugated with IRDye©800 or IRDye©680, respectively, were used at 1:10000. Proteins were
332 visualized using a ChemiDoc Imaging System (BioRad) and the intensity of protein bands was
333 quantified using ImageJ (NIH). To normalize for sample loading, the intensity of total protein
334 (TLP) measured on the TGX Stain-Free™ gels was used as previously described (*55*).

335 **ELISA**

336 Levels of Aβ40 and Aβ42 in hippocampal samples were quantitated by Human/Rat β Amyloid
337 (40) ELISA kit (Wako 294-62501, LOT# WTL5240) and Human/Rat β Amyloid (42) ELISA kit
338 (Wako 290-62601, LOT# WTM4353) respectively. Both ELISAs were performed according to
339 the manufacturer recommendations, and the plates were read at 450 nm using an Eon microplate
340 reader (BioTek).

341 **Immunofluorescence**

342 A Leica Vibratome VT1220S (Leica Microsystems) was used to cut 100 µm coronal sections of
343 paraformaldehyde fixed brain tissue. Sections were rinsed 3 times in 0.1M phosphate-buffered
344 saline with 0.2% Triton X-100 (PBST) for 10 min, blocked for 1 hr with 10% Normal Goat Serum
345 (NGS) in PBST and then incubated for 15 hrs at 4 °C in primary anti-c-Fos (rabbit monoclonal,
346 1:2000, Cell Signaling 2250) diluted in PBST containing 4% NGS. Sections were washed in PBST
347 and subsequently incubated for 2 hrs at room temperature in AlexaFluor™ 488-conjugated goat
348 anti-rabbit (1:500, Invitrogen A11008) diluted in PBST containing 4% NGS. Tissue was mounted

349 on SuperFrost™ slides (Thermo Fisher Scientific 12-550-15) using a fluorescence mounting
350 medium with DAPI (Abcam ab104139) and cover-slipped.
351 All confocal images were acquired with a Zeiss LSM710 confocal laser scanning
352 microscope. Acquisitions were 12-bit images, 2048x2048 pixels with a pixel dwell time of 3.15
353 µs. A 40x Plan-Apochromat oil objective (1.4 NA) was used for magnification. Tile scans were
354 acquired at 12-bits, 512x512 pixels (each tile) with a pixel dwell time of 0.64 µs and an x5 EC-
355 Plan-Neofluar objective (0.16 NA). Laser power, photomultiplier tube (PMT) settings, filters,
356 dichroic mirrors, scanning speed were kept constant for all acquisitions.

357 **Y-maze spatial memory test**

358 The Y-maze apparatus consisted of 3 identical arms (each 36.2 x 8.25 cm) in a Y configuration
359 (placed at 120° to each other) connected by a center polygonal area. The walls of the arms were
360 transparent so the animals could identify two distinct visual cues placed outside the apparatus to
361 facilitate spatial navigation. During the training phase, the mice were placed individually in the
362 maze and left freely to explore two arms, for 10 minutes, while the third arm was blocked by a
363 removable door. An hour later, the mice were returned to the maze and allowed to explore all arms.
364 The latency to enter the new (third) arm was measured for each mouse and used to score the spatial
365 memory performance of the mice. Between mice, the maze was cleaned with 70% isopropyl
366 solution to minimize scent cues. Entry into the arm was defined as a mouse placing all four paws
367 on the arm. For the mice receiving the daily optogenetic stimulation, the spatial memory test was
368 performed after the end of the 4 weeks-long stimulation protocol. The day of the test, the mice
369 receive a 2s light pulse before the beginning of the training phase.

370 **Statistical Analysis**

371 For the proteomic experiments, the statistical analysis of the label-free quantification intensities
372 was performed with Perseus (version 1.6.15) using a two sample t-test with a P-value less than
373 0.05 or an ANOVA for multiple sample tests with a P-value lower than of 0.05. For estimation
374 statistics based on effect size and confidence intervals (*56*), the data were uploaded and analyzed
375 on https://www.estimationstats.com/. The estimation plots show the mean difference between the
376 groups and the 95% confidence interval by the ends of the vertical error bar. Bar graphs were
377 generated with GraphPad Prism 9 (GraphPad software). Circos plots were drawn using RStudio

378 by uploading the list of proteins enriched in our samples for each biological process selected by
379 the gene-ontology analysis.

380 **References**

381 1. G. G. Turrigiano, S. B. Nelson, Homeostatic plasticity in the developing nervous system.
382 *Nat. Rev. Neurosci. 2004 52*. **5**, 97–107 (2004).

383 2. W. Wefelmeyer, C. J. Puhl, J. Burrone, Homeostatic Plasticity of Subcellular Neuronal
384 Structures: From Inputs to Outputs. *Trends Neurosci.* **39**, 656–667 (2016).

385 3. E. Marder, J. M. Goaillard, Variability, compensation and homeostasis in neuron and
386 network function. *Nat. Rev. Neurosci. 2006 77*. **7**, 563–574 (2006).

387 4. N. Specchio, V. Di Micco, M. Trivisano, A. Ferretti, P. Curatolo, The epilepsy-autism
388 spectrum disorder phenotype in the era of molecular genetics and precision therapy.
389 *Epilepsia*. **63**, 6–21 (2022).

390 5. J. J. Palop, L. Mucke, Network abnormalities and interneuron dysfunction in Alzheimer
391 disease. *Nat. Rev. Neurosci.* **17**, 777–792 (2016).

392 6. B. Zott, M. A. Busche, R. A. Sperling, A. Konnerth, What Happens with the Circuit in
393 Alzheimer's Disease in Mice and Humans? *Annu. Rev. Neurosci.* **41**, 277–297 (2018).

394 7. J. V. Andersen, N. H. Skotte, S. K. Christensen, F. S. Polli, M. Shabani, K. H. Markussen,
395 H. Haukedal, E. W. Westi, M. Diaz-delCastillo, R. C. Sun, K. A. Kohlmeier, A.
396 Schousboe, M. S. Gentry, H. Tanila, K. K. Freude, B. I. Aldana, M. Mann, H. S.
397 Waagepetersen, Hippocampal disruptions of synaptic and astrocyte metabolism are
398 primary events of early amyloid pathology in the 5xFAD mouse model of Alzheimer's
399 disease. *Cell Death Dis. 2021 1211*. **12**, 1–13 (2021).

400 8. S. S. Bassett, D. M. Yousem, C. Cristinzio, I. Kusevic, M. A. Yassa, B. S. Caffo, S. L.
401 Zeger, Familial risk for Alzheimer's disease alters fMRI activation patterns. *Brain*. **129**,
402 1229–1239 (2006).

403 9. S. Y. Bookheimer, M. H. Strojwas, M. S. Cohen, A. M. Saunders, M. A. Pericak-Vance, J.
404 C. Mazziotta, G. W. Small, Patterns of Brain Activation in People at Risk for Alzheimer's
405 Disease. *N. Engl. J. Med.* **343**, 450–456 (2000).

406 10. M. A. Busche, G. Eichhoff, H. Adelsberger, D. Abramowski, K.-H. Wiederhold, C. Haass,
407 M. Staufenbiel, A. Konnerth, O. Garaschuk, Clusters of hyperactive neurons near amyloid
408 plaques in a mouse model of Alzheimer's disease. *Science*. **321**, 1686–9 (2008).

409 11. L. Verret, E. O. Mann, G. B. Hang, A. M. I. Barth, I. Cobos, K. Ho, N. Devidze, E.
410 Masliah, A. C. Kreitzer, I. Mody, L. Mucke, J. J. Palop, Inhibitory interneuron deficit
411 links altered network activity and cognitive dysfunction in alzheimer model. *Cell*. **149**,
412 708–721 (2012).

12. K. A. Vossel, M. C. Tartaglia, H. B. Nygaard, A. Z. Zeman, B. L. Miller, Epileptic activity in Alzheimer's disease: causes and clinical relevance. *Lancet Neurol.* **16**, 311–322 (2017).

13. B. Zott, M. M. Simon, W. Hong, F. Unger, H. J. Chen-Engerer, M. P. Frosch, B. Sakmann, D. M. Walsh, A. Konnerth, A vicious cycle of β amyloid−dependent neuronal hyperactivation. *Science (80-.).* **365**, 559–565 (2019).

14. L. M. Ittner, Y. D. Ke, F. Delerue, M. Bi, A. Gladbach, J. van Eersel, H. Wölfing, B. C. Chieng, M. J. Christie, I. A. Napier, A. Eckert, M. Staufenbiel, E. Hardeman, J. Götz, Dendritic function of tau mediates amyloid-beta toxicity in Alzheimer's disease mouse models. *Cell*. **142**, 387–97 (2010).

15. E. D. Roberson, K. Scearce-Levie, J. J. Palop, F. Yan, I. H. Cheng, T. Wu, H. Gerstein, G.-Q. Yu, L. Mucke, Reducing endogenous tau ameliorates amyloid beta-induced deficits in an Alzheimer's disease mouse model. *Science*. **316**, 750–4 (2007).

16. X. W. Huijbers, A. P. Schultz, K. V. Papp, M. R. Lapoint, X. Hanseeuw, X. J. P. Chhatwal, T. Hedden, X. A. Johnson, X. R. A. Sperling, Tau Accumulation in Clinically Normal Older Adults Is Associated with Hippocampal Hyperactivity. *J. Neurosci.* **39**, 548–556 (2019).

17. J. R. Cirrito, K. A. Yamada, M. B. Finn, R. S. Sloviter, K. R. Bales, P. C. May, D. D. Schoepp, S. M. Paul, S. Mennerick, D. M. Holtzman, Synaptic activity regulates interstitial fluid amyloid-beta levels in vivo. *Neuron*. **48**, 913–22 (2005).

18. K. Yamamoto, Z.-I. ichi Tanei, T. Hashimoto, T. Wakabayashi, H. Okuno, Y. Naka, O. Yizhar, L. E. Fenno, M. Fukayama, H. Bito, J. R. Cirrito, D. M. Holtzman, K. Deisseroth, T. Iwatsubo, Chronic Optogenetic Activation Augments Aβ Pathology in a Mouse Model of Alzheimer Disease. *Cell Rep.* **11**, 859–865 (2015).

19. M. L. Frandemiche, S. De Seranno, T. Rush, E. Borel, A. Elie, I. Arnal, F. Lanté, A. Buisson, Activity-Dependent Tau Protein Translocation to Excitatory Synapse Is Disrupted by Exposure to Amyloid-Beta Oligomers. *J. Neurosci.* **34**, 6084–6097 (2014).

20. C. K. Kim, A. Adhikari, K. Deisseroth, Integration of optogenetics with complementary methodologies in systems neuroscience. *Nat. Rev. Neurosci. 2017 184*. **18**, 222–235 (2017).

21. E. S. Ruthazer, J. C. Béïque, Y. De Koninck, Editorial: Shedding Light on the Nervous System: Progress in Neurophotonics Research. *Front. Neural Circuits*. **16**, 49 (2022).

22. L. Fenno, O. Yizhar, K. Deisseroth, The Development and Application of Optogenetics. *https://doi.org/10.1146/annurev-neuro-061010-113817*. **34**, 389–412 (2011).

23. O. Yizhar, L. E. Fenno, M. Prigge, F. Schneider, T. J. Davidson, D. J. O'Shea, V. S. Sohal, I. Goshen, J. Finkelstein, J. T. Paz, K. Stehfest, R. Fudim, C. Ramakrishnan, J. R. Huguenard, P. Hegemann, K. Deisseroth, Neocortical excitation/inhibition balance in information processing and social dysfunction. *Nature*. **477**, 171–8 (2011).

24. H. Oakley, S. L. Cole, S. Logan, E. Maus, P. Shao, J. Craft, A. Guillozet-Bongaarts, M. Ohno, J. Disterhoft, L. Van Eldik, R. Berry, R. Vassar, Intraneuronal β-Amyloid Aggregates, Neurodegeneration, and Neuron Loss in Transgenic Mice with Five Familial Alzheimer's Disease Mutations: Potential Factors in Amyloid Plaque Formation. *J. Neurosci.* **26**, 10129–10140 (2006).

25. Y. LeChasseur, S. Dufour, G. Lavertu, C. Bories, M. Deschênes, R. Vallée, Y. De Koninck, A microprobe for parallel optical and electrical recordings from single neurons in vivo. *Nat. Methods*. **8**, 319–25 (2011).

26. S. Dufour, Y. De Koninck, Optrodes for combined optogenetics and electrophysiology in live animals. *https://doi.org/10.1117/1.NPh.2.3.031205*. **2**, 031205 (2015).

27. A. Garcia-Moreno, R. López-Domínguez, J. A. Villatoro-García, A. Ramirez-Mena, E. Aparicio-Puerta, M. Hackenberg, A. Pascual-Montano, P. Carmona-Saez, Functional Enrichment Analysis of Regulatory Elements. *Biomedicines*. **10** (2022), doi:10.3390/BIOMEDICINES10030590.

28. D. Szklarczyk, A. L. Gable, K. C. Nastou, D. Lyon, R. Kirsch, S. Pyysalo, N. T. Doncheva, M. Legeay, T. Fang, P. Bork, L. J. Jensen, C. von Mering, The STRING database in 2021: customizable protein-protein networks, and functional characterization of user-uploaded gene/measurement sets. *Nucleic Acids Res.* **49**, D605–D612 (2021).

29. A. L. Oblak, P. B. Lin, K. P. Kotredes, R. S. Pandey, D. Garceau, H. M. Williams, A. Uyar, R. O'Rourke, S. O'Rourke, C. Ingraham, D. Bednarczyk, M. Belanger, Z. A. Cope, G. J. Little, S. P. G. Williams, C. Ash, A. Bleckert, T. Ragan, B. A. Logsdon, L. M. Mangravite, S. J. Sukoff Rizzo, P. R. Territo, G. W. Carter, G. R. Howell, M. Sasner, B. T. Lamb, Comprehensive Evaluation of the 5XFAD Mouse Model for Preclinical Testing Applications: A MODEL-AD Study. *Front. Aging Neurosci.* **13**, 431 (2021).

30. B. Bai, X. Wang, Y. Li, P. C. Chen, K. Yu, K. K. Dey, J. M. Yarbro, X. Han, B. M. Lutz, S. Rao, Y. Jiao, J. M. Sifford, J. Han, M. Wang, H. Tan, T. I. Shaw, J. H. Cho, S. Zhou, H. Wang, M. Niu, A. Mancieri, K. A. Messler, X. Sun, Z. Wu, V. Pagala, A. A. High, W. Bi, H. Zhang, H. Chi, V. Haroutunian, B. Zhang, T. G. Beach, G. Yu, J. Peng, Deep Multilayer Brain Proteomics Identifies Molecular Networks in Alzheimer's Disease Progression. *Neuron*. **105**, 975-991.e7 (2020).

31. D. K. Kim, D. Han, J. Park, H. Choi, J. C. Park, M. Y. Cha, J. Woo, M. S. Byun, D. Y. Lee, Y. Kim, I. Mook-Jung, Deep proteome profiling of the hippocampus in the 5XFAD mouse model reveals biological process alterations and a novel biomarker of Alzheimer's disease. *Exp. Mol. Med. 2019 5111*. **51**, 1–17 (2019).

32. A. G. Hinnebusch, I. P. Ivanov, N. Sonenberg, Translational control by 5′-untranslated regions of eukaryotic mRNAs. *Science (80-.).* **352**, 1413–1416 (2016).

33. A. Caccamo, S. Majumder, A. Richardson, R. Strong, S. Oddo, Molecular interplay between mammalian target of rapamycin (mTOR), amyloid-β, and Tau: Effects on cognitive impairments. *J. Biol. Chem.* **285**, 13107–13120 (2010).

490 34. A. Garami, F. J. T. Zwartkruis, T. Nobukuni, M. Joaquin, M. Roccio, H. Stocker, S. C.
491 Kozma, E. Hafen, J. L. Bos, G. Thomas, Insulin activation of Rheb, a mediator of
492 mTOR/S6K/4E-BP signaling, is inhibited by TSC1 and 2. *Mol. Cell*. **11**, 1457–1466
493 (2003).

494 35. I. Keramidis, B. B. McAllister, J. Bourbonnais, F. Wang, D. Isabel, E. Rezaei, R.
495 Sansonetti, P. Degagne, J. P. Hamel, M. Nazari, S. Inayat, J. C. Dudley, A. Barbeau, L.
496 Froux, A. G. Godin, M. H. Mohajerani, Y. De Koninck, Restoring neuronal chloride
497 extrusion reverses cognitive decline linked to Alzheimer's disease mutations. *Brain*
498 (2023), doi:10.1093/BRAIN/AWAD250.

499 36. F. Kamenetz, T. Tomita, H. Hsieh, G. Seabrook, D. Borchelt, T. Iwatsubo, S. Sisodia, R.
500 Malinow, APP Processing and Synaptic Function. *Neuron*. **37**, 925–937 (2003).

501 37. A. W. Bero, A. Q. Bauer, F. R. Stewart, B. R. White, J. R. Cirrito, M. E. Raichle, J. P.
502 Culver, D. M. Holtzman, Bidirectional Relationship between Functional Connectivity and
503 Amyloid-β Deposition in Mouse Brain. *J. Neurosci.* **32**, 4334–4340 (2012).

504 38. D. Putcha, M. Brickhouse, K. O'Keefe, C. Sullivan, D. Rentz, G. Marshall, B. Dickerson,
505 R. Sperling, Hippocampal Hyperactivation Associated with Cortical Thinning in
506 Alzheimer's Disease Signature Regions in Non-Demented Elderly Adults. *J. Neurosci.* **31**,
507 17680–17688 (2011).

508 39. M. T. Koh, R. P. Haberman, S. Foti, T. J. McCown, M. Gallagher, Treatment strategies
509 targeting excess hippocampal activity benefit aged rats with cognitive impairment.
510 *Neuropsychopharmacology*. **35**, 1016–1025 (2010).

511 40. R. A. Sperling, P. S. Laviolette, K. O'Keefe, J. O'Brien, D. M. Rentz, M. Pihlajamaki, G.
512 Marshall, B. T. Hyman, D. J. Selkoe, T. Hedden, R. L. Buckner, J. A. Becker, K. A.
513 Johnson, Amyloid deposition is associated with impaired default network function in older
514 persons without dementia. *Neuron*. **63**, 178–88 (2009).

515 41. N. Oser, M. Hubacher, K. Specht, A. N. Datta, P. Weber, I. K. Penner, Default mode
516 network alterations during language task performance in children with benign epilepsy
517 with centrotemporal spikes (BECTS). *Epilepsy Behav.* **33**, 12–17 (2014).

518 42. L. J. Seidman, I. M. Rosso, H. W. Thermenos, N. Makris, R. Juelich, J. D. E. Gabrieli, S.
519 V. Faraone, M. T. Tsuang, S. Whitfield-Gabrieli, Medial temporal lobe default mode
520 functioning and hippocampal structure as vulnerability indicators for schizophrenia: A
521 MRI study of non-psychotic adolescent first-degree relatives. *Schizophr. Res.* **159**, 426–
522 434 (2014).

523 43. S. L. Miller, K. Celone, K. DePeau, E. Diamond, B. C. Dickerson, D. Rentz, M.
524 Pihlajamäki, R. A. Sperling, Age-related memory impairment associated with loss of
525 parietal deactivation but preserved hippocampal activation. *Proc. Natl. Acad. Sci. U. S. A.*
526 **105**, 2181–2186 (2008).

527 44. A. Bakker, G. L. Krauss, M. S. Albert, C. L. Speck, L. R. Jones, C. E. Stark, M. A. Yassa,

528 S. S. Bassett, A. L. Shelton, M. Gallagher, Reduction of Hippocampal Hyperactivity
529 Improves Cognition in Amnestic Mild Cognitive Impairment. *Neuron*. **74**, 467–474
530 (2012).

531 45. F. E. Henry, X. Wang, D. Serrano, A. S. Perez, C. J. L. Carruthers, E. L. Stuenkel, M. A.
532 Sutton, A Unique Homeostatic Signaling Pathway Links Synaptic Inactivity to
533 Postsynaptic mTORC1. *J. Neurosci.* **38**, 2207–2225 (2018).

534 46. P. N. Lacor, M. C. Buniel, P. W. Furlow, A. S. Clemente, P. T. Velasco, M. Wood, K. L.
535 Viola, W. L. Klein, Aβ Oligomer-Induced Aberrations in Synapse Composition, Shape,
536 and Density Provide a Molecular Basis for Loss of Connectivity in Alzheimer's Disease.
537 *J. Neurosci.* **27**, 796–807 (2007).

538 47. J. K. Hefendehl, J. LeDue, R. W. Y. Ko, J. Mahler, T. H. Murphy, B. A. MacVicar,
539 Mapping synaptic glutamate transporter dysfunction in vivo to regions surrounding Aβ
540 plaques by iGluSnFR two-photon imaging. *Nat. Commun. 2016 71*. **7**, 1–13 (2016).

541 48. M. A. Busche, M. Kekuš, H. Adelsberger, T. Noda, H. Förstl, I. Nelken, A. Konnerth,
542 Rescue of long-range circuit dysfunction in Alzheimer's disease models. *Nat. Neurosci.*
543 **18**, 1623–1630 (2015).

544 49. R. L. Buckner, A. Z. Snyder, B. J. Shannon, G. LaRossa, R. Sachs, A. F. Fotenos, Y. I.
545 Sheline, W. E. Klunk, C. A. Mathis, J. C. Morris, M. A. Mintun, Molecular, Structural,
546 and Functional Characterization of Alzheimer's Disease: Evidence for a Relationship
547 between Default Activity, Amyloid, and Memory. *J. Neurosci.* **25**, 7709–7717 (2005).

548 50. B. Styr, I. Slutsky, Imbalance between firing homeostasis and synaptic plasticity drives
549 early-phase Alzheimer's disease. *Nat. Neurosci.* **21**, 463–473 (2018).

550 51. D. J. Selkoe, Alzheimer's Disease: Genes, Proteins, and Therapy. *Physiol. Rev.* **81**, 741–
551 766 (2001).

552 52. S. L. Jackman, C. H. Chen, S. N. Chettih, S. Q. Neufeld, I. R. Drew, C. K. Agba, I.
553 Flaquer, A. N. Stefano, T. J. Kennedy, J. E. Belinsky, K. Roberston, C. C. Beron, B. L.
554 Sabatini, C. D. Harvey, W. G. Regehr, Silk Fibroin Films Facilitate Single-Step Targeted
555 Expression of Optogenetic Proteins. *Cell Rep.* **22**, 3351–3361 (2018).

556 53. C. S. Hughes, S. Moggridge, T. Müller, P. H. Sorensen, G. B. Morin, J. Krijgsveld,
557 Single-pot, solid-phase-enhanced sample preparation for proteomics experiments. *Nat.*
558 *Protoc. 2018 141*. **14**, 68–85 (2018).

559 54. S. Tyanova, T. Temu, P. Sinitcyn, A. Carlson, M. Y. Hein, T. Geiger, M. Mann, J. Cox,
560 The Perseus computational platform for comprehensive analysis of (prote)omics data. *Nat.*
561 *Methods*. **13**, 731–740 (2016).

562 55. S. C. Taylor, T. Berkelman, G. Yadav, M. Hammond, A defined methodology for reliable
563 quantification of western blot data. *Mol. Biotechnol.* **55**, 217–226 (2013).

564 56. J. Ho, T. Tumkaya, S. Aryal, H. Choi, A. Claridge-Chang, Moving beyond P values: data

565 analysis with estimation graphics. *Nat. Methods 2019 167*. **16**, 565–566 (2019).

566 57. Y. Perez-Riverol, J. Bai, C. Bandla, D. García-Seisdedos, S. Hewapathirana, S.
567 Kamatchinathan, D. J. Kundu, A. Prakash, A. Frericks-Zipper, M. Eisenacher, M. Walzer,
568 S. Wang, A. Brazma, J. A. Vizcaíno, The PRIDE database resources in 2022: a hub for
569 mass spectrometry-based proteomics evidences. *Nucleic Acids Res.* **50**, D543–D552
570 (2022).

571

572 **Acknowledgments**

573 The authors thank Camille Sugère and Lyane Méthot for assistance with the daily optogenetic
574 stimulation protocol and Drs Efthimios MC Skoulakis and Nicolò Ilacqua for their invaluable
575 comments on the proteomics data. The authors also thank Dominique Isabel for assistance with
576 RStudio and data visualization.

577 **Funding:**

578 Weston Family Foundation Transformation Research grant TR192089 (YDK)
579 Canadian Institutes of Health Research (CIHR) grant FDN - 159906 (YDK)
580 Canada Research Chair program (YDK)
581 Université Laval Norampac Research grant on Alzheimer's disease and Related Diseases (IK)
582 Université Laval Fondation De La Famille Lemaire research grant on Alzheimer's disease and
583 Related Diseases (IK)

584 **Author contributions:**

585 Conceptualization: IK, KP, YDK
586 Methodology: IK, MS, JA, KP, YDK
587 Investigation: IK, MS, RS, JA
588 Visualization: IK, KP, YDK
589 Supervision: KP, YDK
590 Writing—original draft: IK, KP, YDK
591 Writing—review & editing: IK, MS, KP, YDK

592 **Competing interests:**

593 All other authors declare they have no competing interests.

594 **Data and materials availability:**

595 The mass spectrometry proteomics data have been deposited to the ProteomeXchange Consortium
596 via the PRIDE (*57*) partner repository with the dataset identifier PXD044437. The code used to

generate the circos plot is available upon request. Any additional information required to reanalyze the data reported in this paper is available from the corresponding author upon request.

Figures

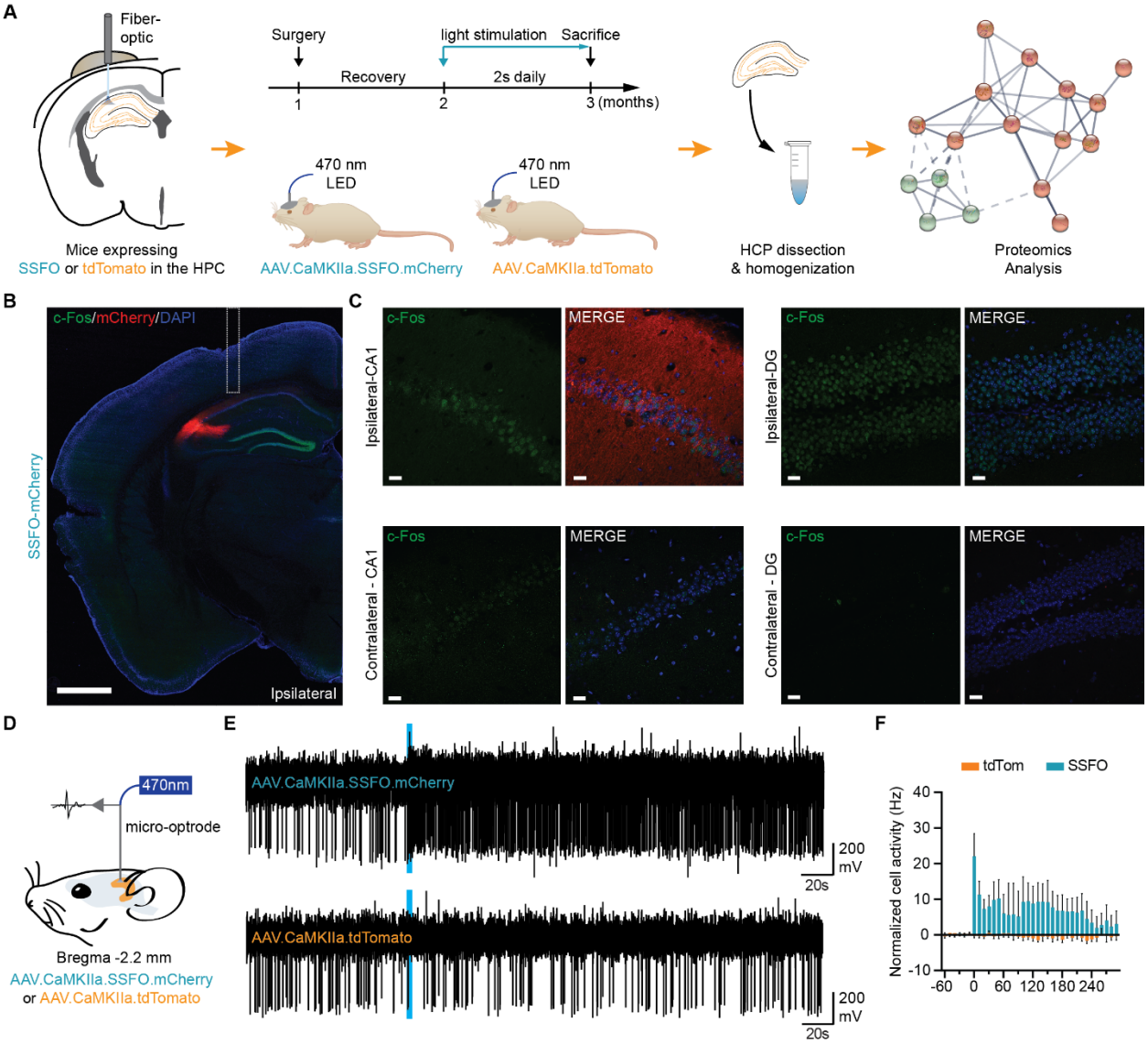

Fig. 1: SSFO optogenetic stimulation activates hippocampal neurons and evokes neuronal hyperactivity. (**A**) Diagram showing an overview of the proteome experiment following chronic optogenetic stimulation of the hippocampus (HPC). (**B** - **C**) Confocal images showing immunofluorescence labeling of c-Fos (green) and mCherry (virus expression reporter protein, red) in coronal sections of mice infected with AAV-SSFO (Scale bars: 1 mm in **B** and 20 µm in **C**; DAPI in blue). Expression of SSFO was observed in the ipsilateral side of infection, but not the contralateral side. Unilateral light stimulation increased the levels of c-Fos at ipsilateral CA1 and DG but not the contralateral side. (**D**) Micro-optrode recording configuration. A 470 nm laser was coupled to an optrode probe for electrical recordings and advanced into the brain. (**E**) Example

610 traces recorded in AAV-SSFO (top) or AAV-tdTomato (bottom) infected mice. 470 nm activation
611 pulse is indicated with a blue bar. (**F**) Peristimulus time histogram of the mean cell activity of
612 neurons recorded from mice infected with AAV-SSFO (n = 10; cyan) or AAV-tdTomato (n = 6;
613 orange). Data presented as mean ± SEM.

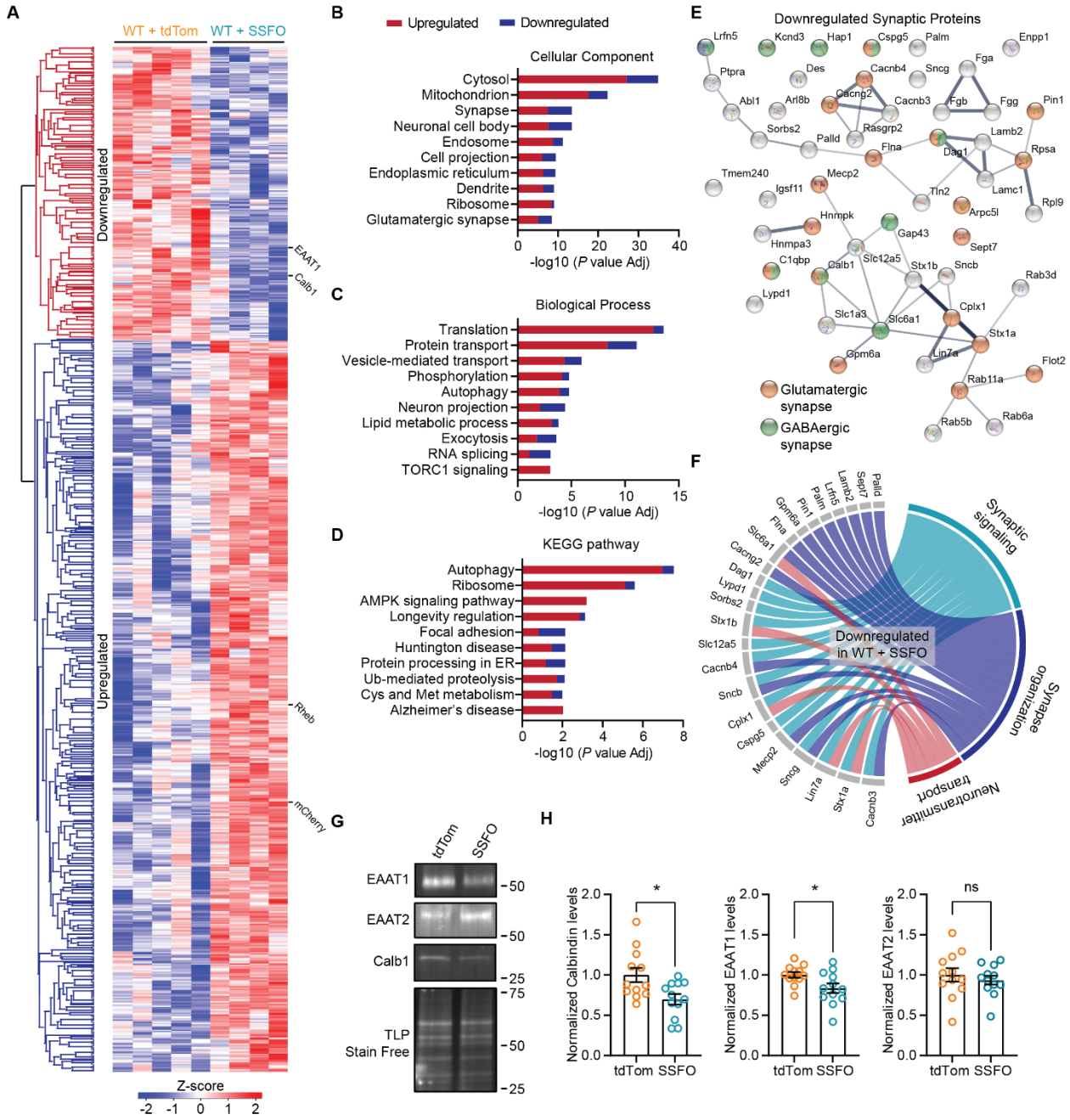

Fig. 2: Chronic optogenetic stimulation elicits synaptic signalling protein downregulation in wild-type mice. (**A**) Heat map illustrating the clustering of proteins (P value ≤ 0.05) in the hippocampus of WT mice expressing SSFO or tdTomato after 4 weeks of daily optogenetic stimulation. The color-coded scale (Z-score) denotes the upregulated (red) and downregulated (blue) proteins. (**B - D**) Results of the GO enrichment analysis of the top 10 most abundant cellular components (**B**), biological processes (**C**) and KEGG pathways (**D**) in the hippocampus of WT+SSFO mice. In red or blue the fraction of the total proteins upregulated or downregulated,

respectively, for each GO-term. (**E**) Interactome of functional or physical protein to protein associations of the synaptic proteins found downregulated in WT+SSFO mice. The proteins in orange are associated with glutamatergic synapses while the proteins in green with GABAergic. (**F**) Circos plots showing the proteins and selected biological processes downregulated in WT+SSFO mice. (**G**) Representative immunoblots for the levels of Calbindin (Calb1), EAAT1 and EAAT2 in hippocampal lysates from WT+SSFO and WT+tdTom mice. (**H**) Quantification of Calbindin, EAAT1 and EAAT2 protein levels measured by immunoblotting in WT+SSFO (cyan; n = 12) and WT+tdTom (orange; n = 12) mice after chronic optogenetic stimulation. The total protein (TLP) levels measured on TGX Stain-Free gels is the loading control.

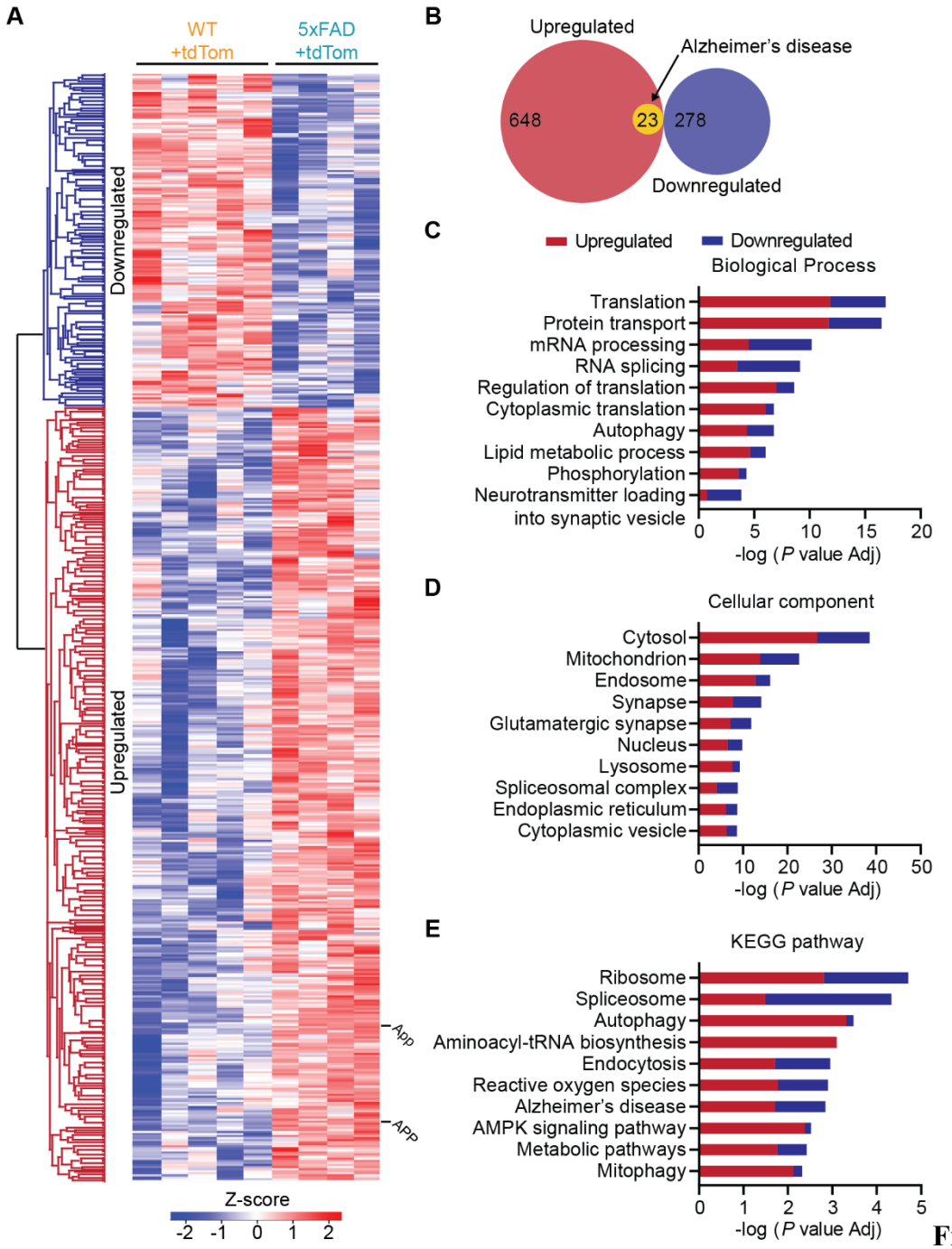

Fig. 3: Early AD pathology alters translation, phosphorylation and autophagy in the hippocampus of 5xFAD mice. (**A**) Heat map illustrating the scaled protein levels in the hippocampus of 3-month-old 5xFAD mice. The color-coded scale (Z-score) denotes the upregulated (red) and downregulated (blue) proteins. (**B**) Venn diagram showing the number of upregulated (red) and downregulated (blue) proteins in 5xFAD mice. In yellow the number of upregulated proteins found enriched in the AD KEGG pathway. (**C - E**) The results of the GO enrichment analysis of

638 the top 10 most abundant biological processes (**C**), cellular components (**D**) and KEGG
639 pathways (**E**) in the hippocampus of 5xFAD mice. The colors in each bar represent the fraction
640 of the total proteins for each GO-term found upregulated (red) or downregulated (blue).

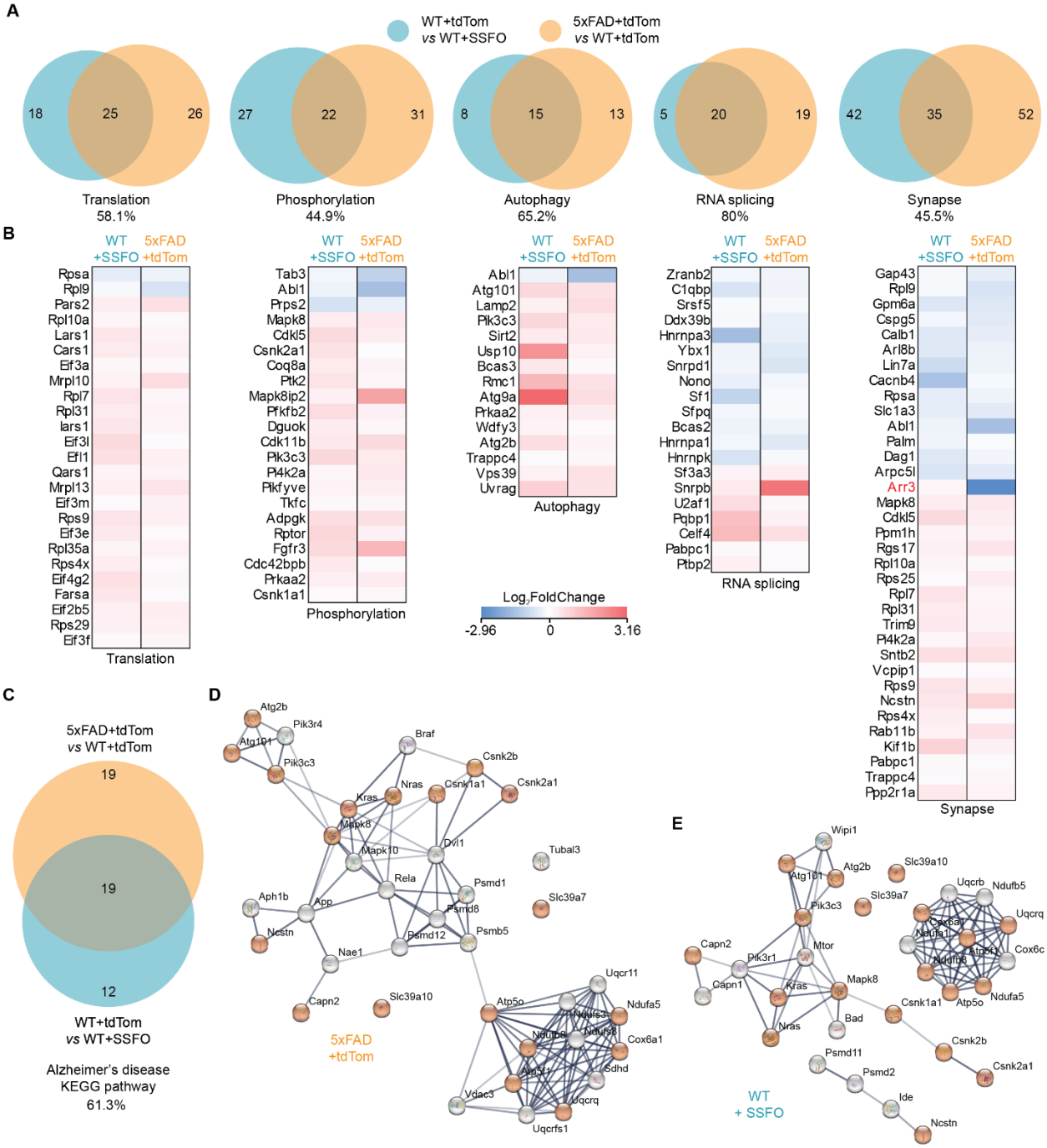

641

642 **Fig. 4: Chronic optogenetic activation of the hippocampus in wild-type mice induces**
643 **proteome changes involved in the early AD pathogenesis.** (**A**) Venn diagrams illustrating the
644 number of the abundant proteins for each GO-term found in the hippocampus of WT+SSFO and
645 5xFAD+tdTom mice. The percentages represent the fraction of the WT+SSFO altered proteins
646 commonly found altered in the 5xFAD mice. (**B**) Heat maps revealing the fold of change in levels
647 for the common proteins of each GO-term in **A** in the WT+SSFO or 5xFAD+tdTom mice. (**C**) The

648 number of common proteins participating in the AD KEGG pathway when comparing the altered
649 proteins in the 5xFAD mice and the proteins altered in the WT+SSFO after the chronic optogenetic
650 stimulation. (**D - E**) Interactomes of functional or physical protein to protein associations of the
651 AD KEGG pathway proteins found altered in 5xFAD+tdTom (**D**) and WT+SSFO (**E**) mice.

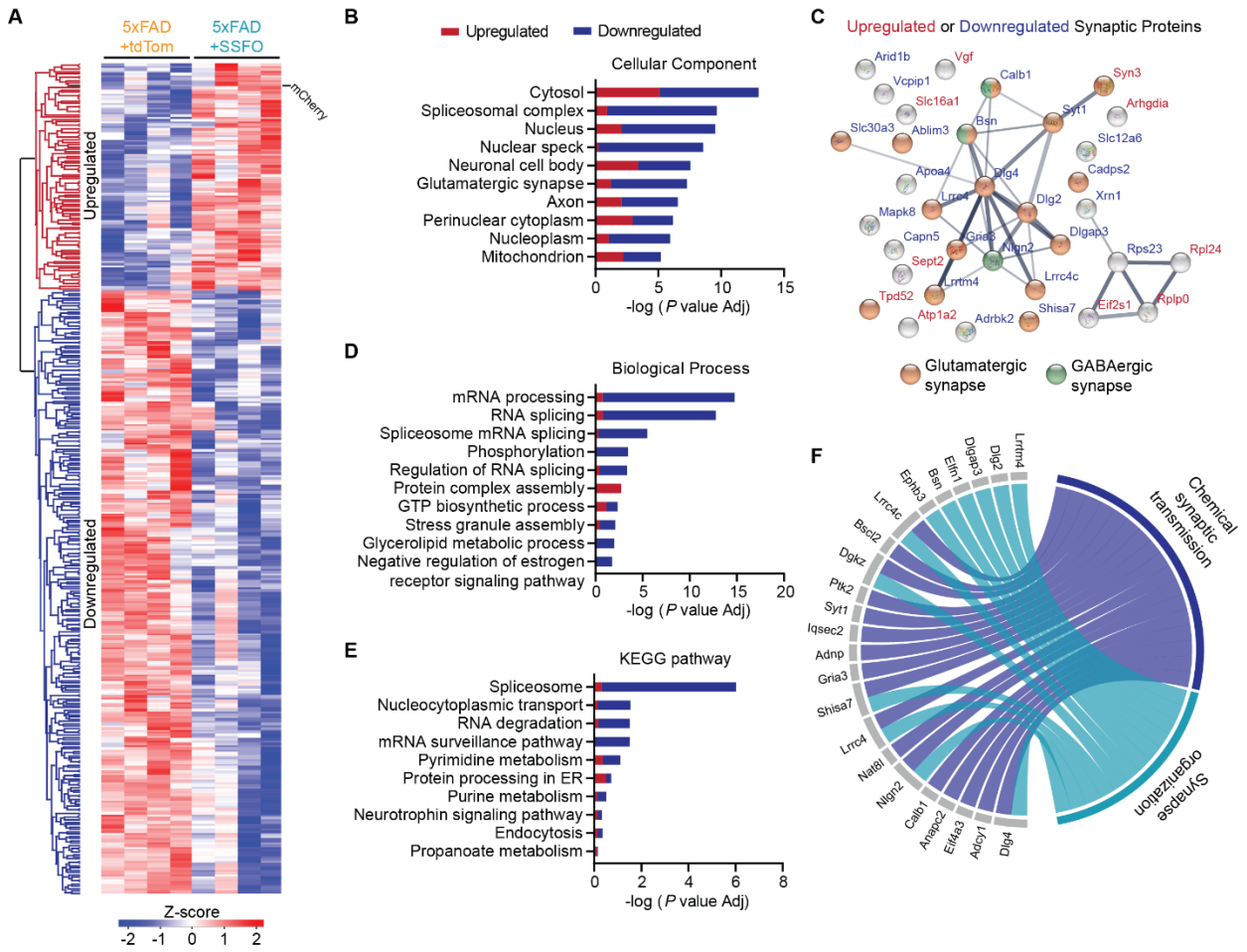

Fig. 5: Chronic optogenetic stimulation downregulates RNA processing and protein phosphorylation in 5xFAD mice. (**A**) Heat map revealing the scaled protein levels in the hippocampus of 5xFAD mice expressing SSFO or tdTomato after 4 weeks of daily optogenetic stimulation. (**B**) GO enrichment analysis showing the top 10 most abundant biological processes. In red or blue the fraction of the total proteins upregulated or downregulated for each GO-term, respectively (**C**) Interactome of functional or physical protein to protein associations of the synaptic proteins altered in 5xFAD+SSFO mice after optogenetic stimulation. The orange circles represent glutamatergic synapse proteins while the green GABAergic. The proteins written in red are upregulated while the proteins in blue are downregulated. (**D - E**) Same as in **B** but for the top 10 cellular components (**D**) and KEGG pathways (**E**) in the hippocampus of 5xFAD+SSFO mice. (**F**) Circos plots showing selected biological processes and the proteins altered in 5xFAD+SSFO mice.

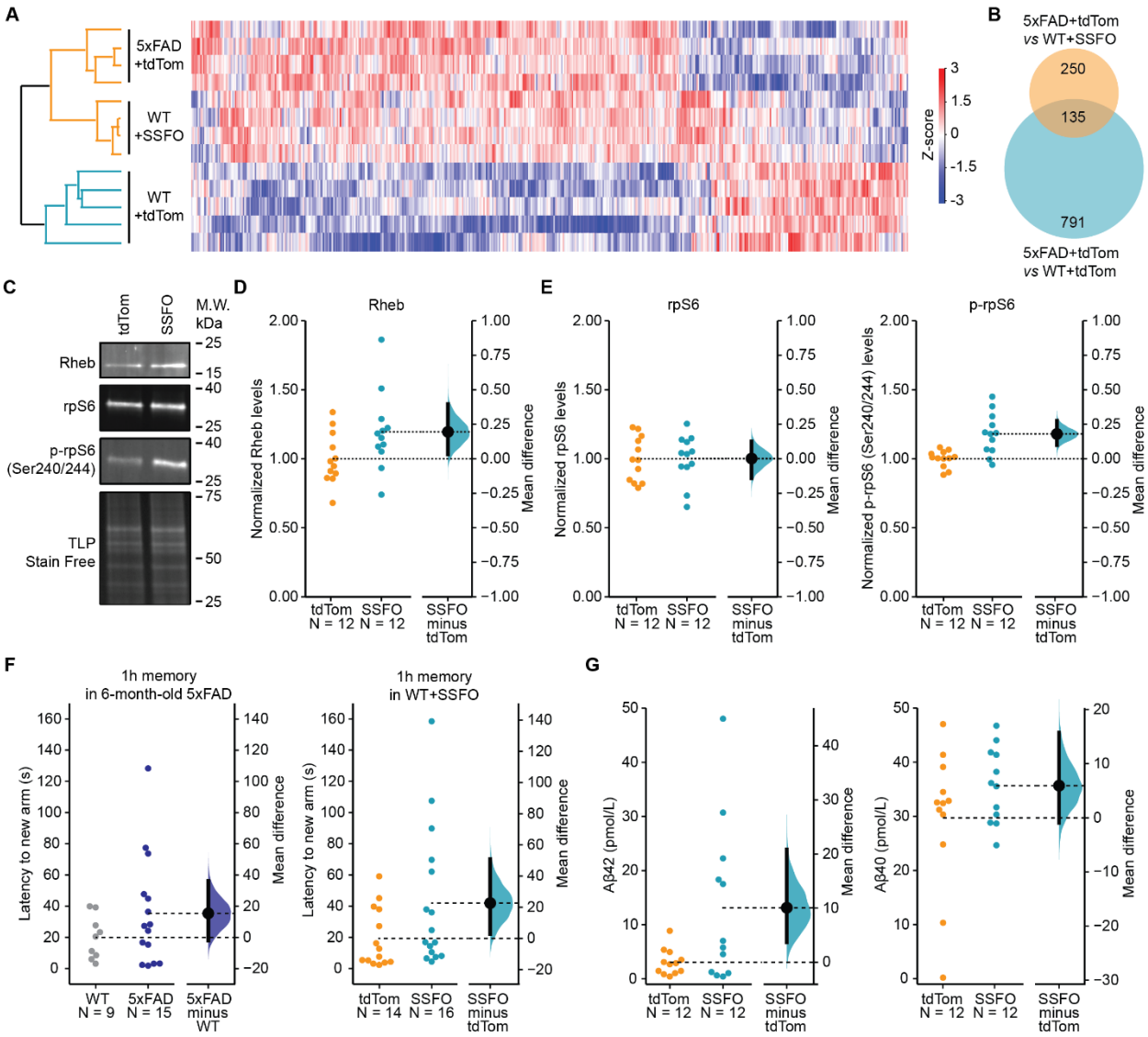

Fig. 6: Chronic hippocampal optogenetic activation induces spatial memory deficits and augments Aβ42 secretion in wild-type mice. (**A**) Heat map revealing the hierarchical clustering of 5xFAD and WT mice expressing SSFO or tdTomato based on their scaled protein levels in the hippocampus after 4 weeks of daily optogenetic stimulation. (**B**) Venn diagram showing the number of common proteins when comparing the altered proteins in 5xFAD mice as compared to WT (5xFAD+tdTom *vs* WT+tdTom) and the proteins altered between the 5xFAD+tdTom and the WT+SSFO. (**C**) Representative immunoblots of hippocampal lysates from WT+SSFO and WT+tdTom mice. (**D**) The protein levels of Rheb in WT+SSFO and WT+tdTom mice. (**E**) Quantification of ribosomal protein S6 (rpS6) expression (left) and its phosphorylation levels at the Ser240/204 residues. (**F**) The latency to the new arm during the one-hour Y-maze spatial

memory test for 6-month-old 5xFAD mice (*n* = 15) *vs* their non-transgenic littermates (WT; *n* = 9) on the left and for WT+SSFO mice (*n* =12) *vs* WT+tdTom mice (*n* = 12) on the right. (**G**) The concentration of soluble Aβ42 (left) and Aβ40 (right) in the hippocampus of WT+SSFO mice as compared to WT+tdTom. The data are analyzed with estimation statistics. Each point represents an individual mouse. The mean difference is dissipated as a dot and the 95% confidence interval by the ends of the vertical error bars.

Supplementary Materials

Figures S1 to S3
Tables S1 to S3
Data S1 to S3

Supplementary Materials for

Chronic optogenetic activation of hippocampal pyramidal neurons replicates the proteome footprint of Alzheimer's disease-like pathology

Iason Keramidis et al.

*Corresponding author. Yves De Koninck Email: yves.dekoninck@neuro.ulaval.ca

This PDF file includes:

Figs. S1 to S3
Tables S1 to S3
Data S1 to S3

694 **Supplementary Figures**

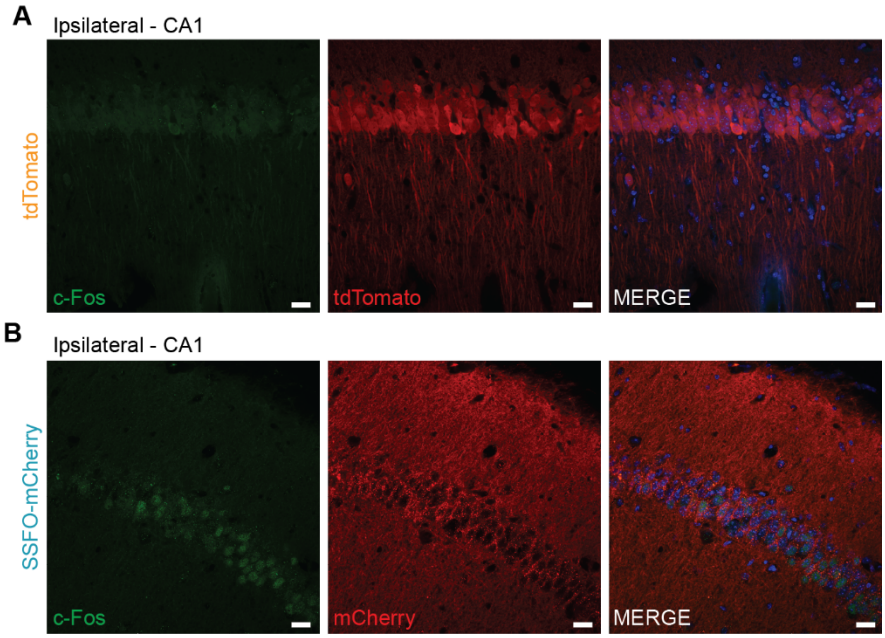

695

696 **Fig. S1. c-Fos expression in the hippocampus of AAV-CaMKIIa-tdTomato or AAV-**
697 **CaMKIIa-SSFO-mCherry infected mice**. (**A**) Confocal images showing labeling for c-Fos
698 (green) and tdTomato (reporter protein, red) in coronal sections of mice infected with AAV-
699 CaMKIIa-tdTomato. (**B**) Confocal images showing labeling for c-Fos (green) and Cherry (SSFO
700 expression reporter protein, red) in coronal sections of mice infected with AAV-CaMKIIa-SFFO.
701 Scale bars 20 µm, DAPI in blue.

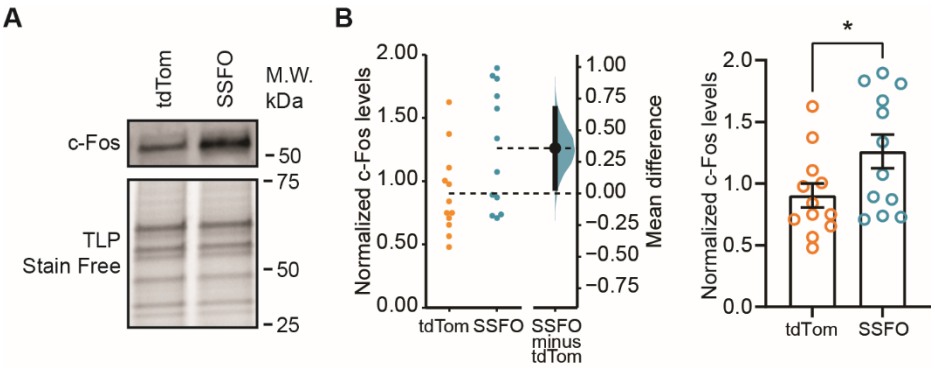

Fig. S2. c-Fos is upregulated in the hippocampus of SSFO expressing wildtype mice. (**A**) Representative immunoblots for the levels of c-Fos in hippocampal samples from WT+tdTom and WT+SSFO mice. (**B**) Quantification of c-Fos protein levels measured by immunoblotting in WT+SSFO (cyan; n = 12) and WT+tdTom (orange; n = 12) mice. Data are represented as the mean difference (dot) and the 95% confidence interval (by the ends of the error bars; left) or as mean ± SEM (right). *P < 0.05.

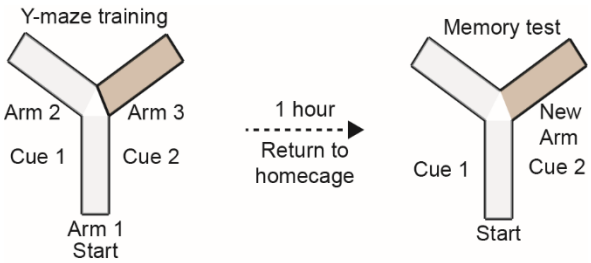

Fig. S3. Y-maze spatial memory test. Schematic representation of the modified version of the Y-maze alternation test for assessing short-term spatial memory performance in rodents.

712 ## Supplementary Tables

713 **Table S1. The differentially expressed proteins upon chronic optogenetic stimulation of the**
714 **hippocampus in wildtype mice.** Proteins are identified by their gene name together with their
715 UniProt ID number. Average log2 fold differences and P-values have been calculated as described
716 in Methods. The log2 fold change becomes positive when WT+SSFO > WT+tdTom and negative
717 when WT+SSFO < WT+tdTom. P-value determines the statistical significance (*P < 0.05).
718
719 **Table S2. Differentially regulated proteins in the hippocampus of 3-month-old 5xFAD.** Gene
720 names and UniProt ID number are used to identify proteins. The log2 fold change becomes positive
721 when 5xFAD+tdTom > WT+tdTom and negative when 5xFAD+tdTom < WT+tdTom. P-value
722 determines the statistical significance (*P < 0.05).
723
724 **Table S3. The proteins altered in levels in the hippocampus of 5xFAD mice upon chronic**
725 **optogenetic stimulation.** Proteins are identified by their gene name and their UniProt ID number
726 is provided. The log2 fold change becomes positive when 5xFAD+SSFO > 5xFAD+tdTom and
727 negative when 5xFAD+SSFO < 5xFAD+tdTom. P-value determines the statistical significance
728 (*P < 0.05).

729 **Supplementary Data**

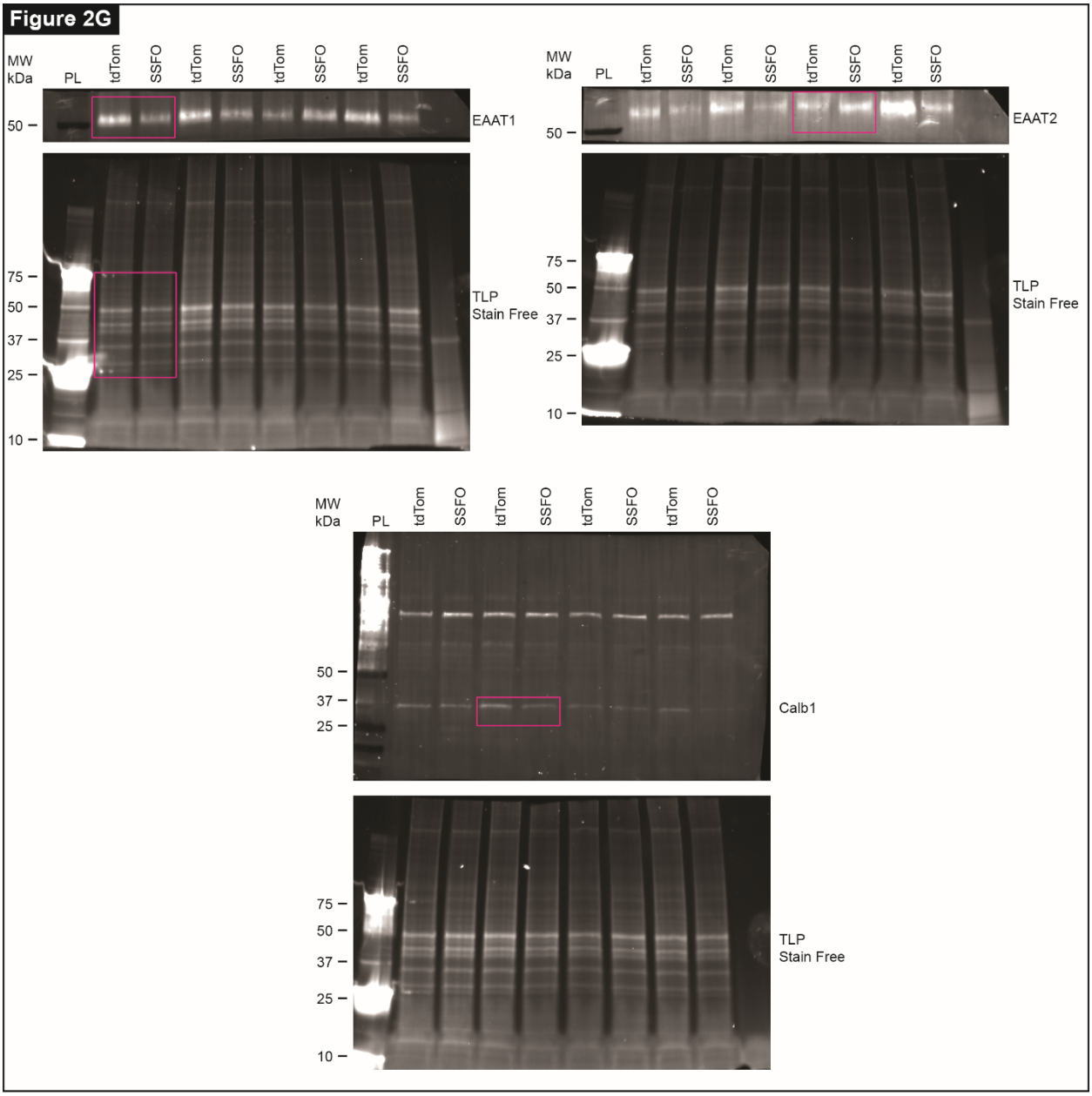

730

731 **Data S1. Original, uncropped immunoblots and TGX Stain Free gels related to Fig. 2**

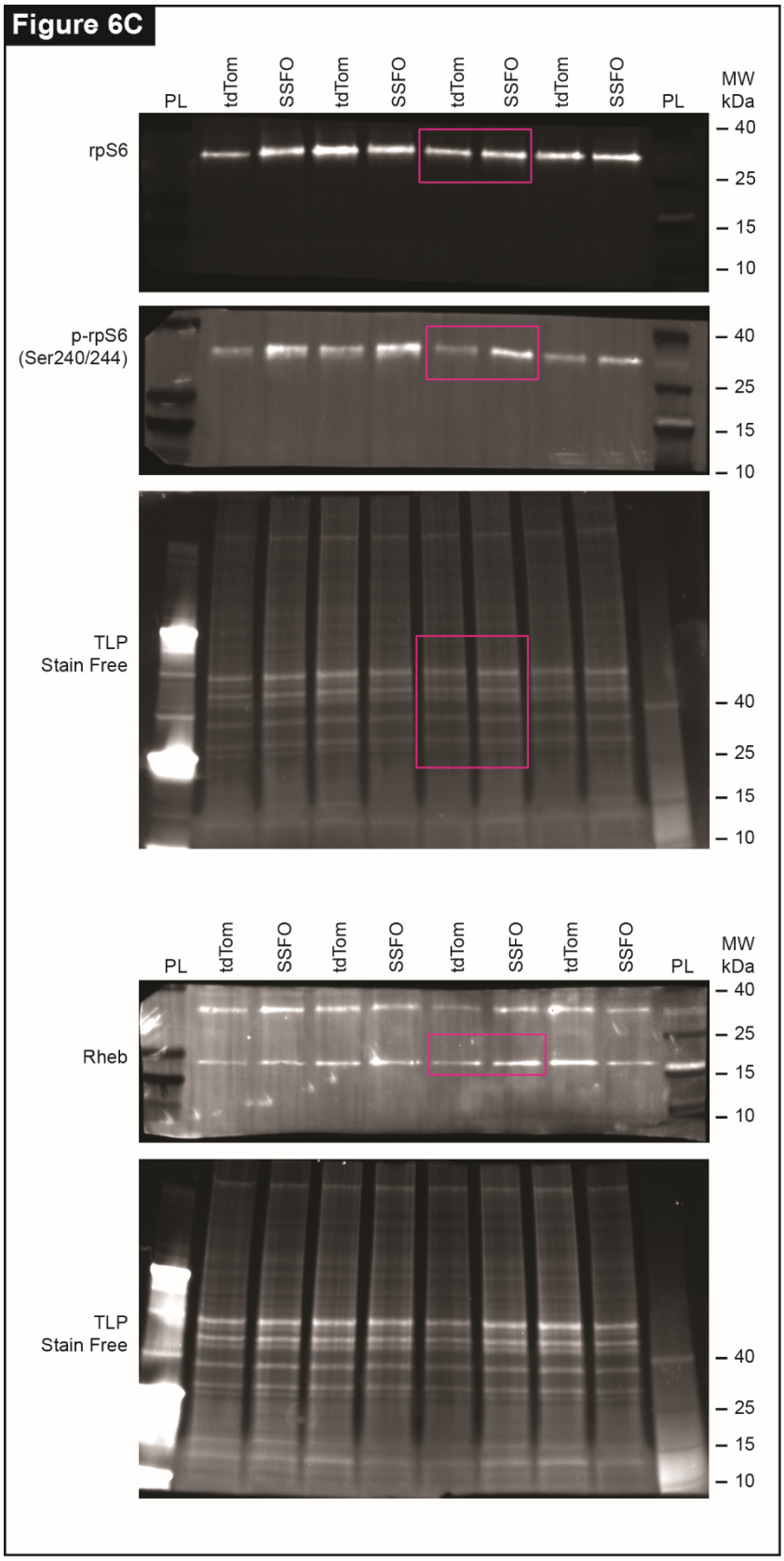

732

733 **Data S2. Original, uncropped immunoblots and TGX Stain Free gels related to Fig. 6**

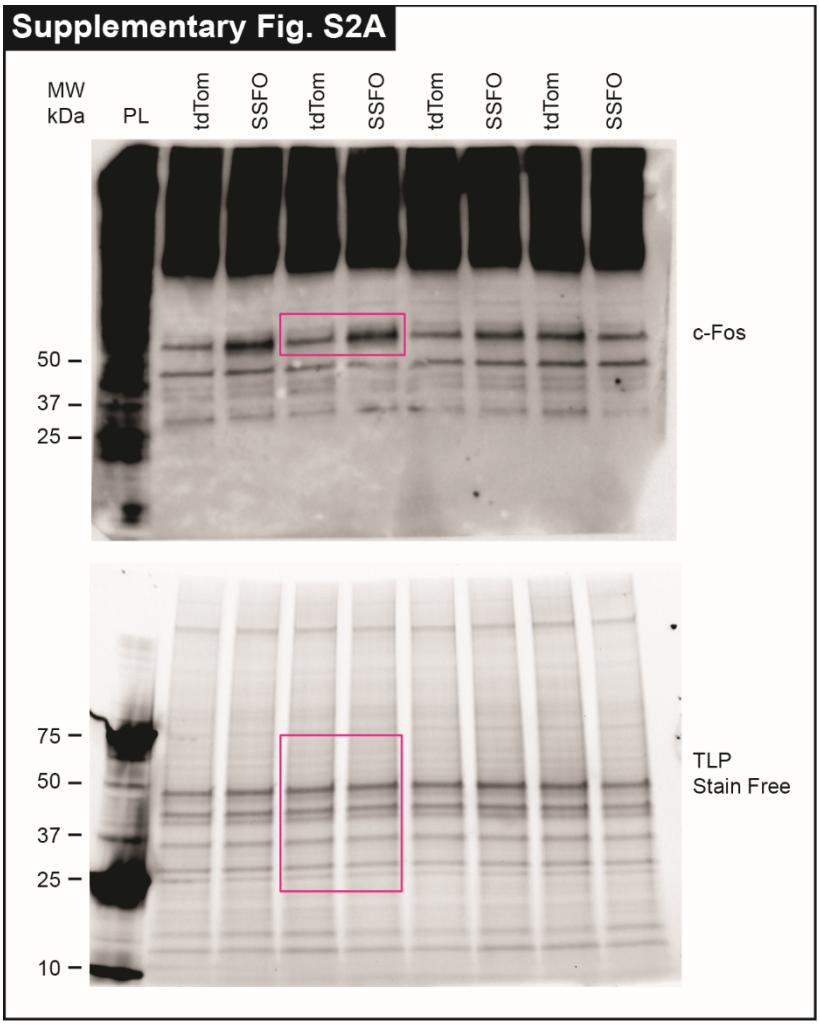

Data S3. Original, uncropped immunoblots and TGX Stain Free gels related to Fig. S2